



RESEARCH ARTICLE

Robust centroid extraction using the hybrid genetic algorithm with applications to planetary optical navigation

Qichang Qiang,^{1,2,3} Baojun Lin,^{1,2,3,4*} and Yingchun Liu^{1,2,3}

¹Innovation Academy for Microsatellites of Chinese Academy of Sciences, Shanghai, China

²University of Chinese Academy of Sciences, Beijing, China

³Shanghai Engineering Center for Microsatellites, Shanghai, China

⁴School of Information Science and Technology, Shanghai Tech University, Shanghai, China.

*Corresponding author. Baojun Lin; Email: LinbJun@126.com

Received: 15 November 2022; **Revised:** 30 November 2024; **Accepted:** 6 January 2025

Keywords: optical navigation; RANSAC; hybrid genetic algorithm; ellipse fitting; centroid extraction

Abstract

Traditional radiometric tracking navigation increasingly fails to meet the demands of deep space exploration. In contrast, optical navigation enables interplanetary spacecraft to navigate autonomously with higher precision. The effectiveness of image processing algorithms plays a crucial role in determining the accuracy of optical navigation systems. This paper presents a robust centroid extraction method based on a hybrid genetic algorithm. First, noise interference is effectively reduced by leveraging proximity information. Second, a fitness evaluation mechanism is introduced to assess model performance throughout the iterative process. Third, an annealing mutation operator is incorporated to prevent premature convergence to local optima. Finally, extensive comparative testing demonstrates that the proposed method offers substantial improvements in both accuracy and robustness, thereby substantially improving the reliability of the navigation system under complex conditions.

1. Introduction

In March 2019, the United States announced the Artemis programme, which aims to facilitate humanity's return to the Moon. The primary goal of this initiative is to establish a permanent and sustainable human presence in cislunar space, while simultaneously preparing for future crewed missions to Mars. To ensure astronaut safety, manned missions must be equipped with autonomous navigation systems to prevent communication loss with ground control. In response to this need, Artemis I has been outfitted with an optical navigation (OpNav) system, specifically designed to enable fully autonomous navigation and ensure the safe return of astronauts to Earth without reliance on the ground station.

In May 1971, the Mariner-9 spacecraft provided the first successful confirmation that the OpNav system could effectively guide spacecraft autonomously during its mission to Mars (Masursky, 1973). Four years later, the viability of this technology was further demonstrated by two Viking missions to Mars (Hess et al., 1977). Initially, however, the OpNav system required ongoing communication with ground stations for mission management and navigation corrections. A significant milestone was reached in 1998 when the Deep Space-1 mission successfully carried out OpNav without relying on ground-based support, marking a major advancement in deep space navigation technology (Bhaskaran et al., 2000). Following this achievement, OpNav capabilities have been incorporated into a range of subsequent missions, such as the Surveyor and the Deep Impact missions (Albee et al., 2001; A'Hearn et al., 2005).

1.1. Related work

The OpNav system utilises various image processing (IP) techniques to extract navigation data from the original images. These observations include landmark tracking (Cheng et al., 2003; Hanak, 2009; Gaskell, 2011; Rohrschneider 2011), star horizon (Synnott et al., 1986; Owen, 2011), centroid and apparent diameter (CAD) (Christian and Lightsey, 2012; Mortari et al., 2013; Borissov and Mortari, 2014), and star occultation (Psiaki and Hinks, 2007). When the probe approaches a planet, landmark tracking methods are often employed to autonomously determine its orbit. However, these methods struggle to accurately capture terrain geometry at greater distances, resulting in unacceptable levels of precision. Conversely, when the probe is farther from the planet, planetary horizon features can be easily extracted for autonomous navigation. While horizon-based navigation typically offers lower accuracy compared to landmark tracking, it still meets the navigational requirements of deep space exploration. Moreover, this approach is more practical in real-world applications, as it does not require identifying and matching specific features.

In horizon-based measurements, CAD observations provide continuous estimates for the detector. These observations consist of two key components: the line of sight (LOS) direction from the camera to the planet and the apparent size of the planet within the image frame. If IP techniques successfully identify the centroid of an object, the LOS direction can be determined. Furthermore, since planetary size and shape are known parameters, measuring the apparent diameter on the image plane allows for the calculation of the distance between the camera and the planet. By integrating these two pieces of information – the LOS direction and apparent diameter – it becomes possible to accurately estimate both the camera position and the spacecraft's location.

Celestial geometric model fitting plays a pivotal role in IP tasks aimed at acquiring CAD observations within OpNav systems. Liu et al. (2020) proposed a real-time ellipse detection algorithm that improves fitting accuracy through edge screening and aggregation, but it struggles with overlapping and complex backgrounds. To address this issue, Panagiotakis and Argyros (2020) developed the RFOVE method, which uses region-based analysis to mitigate overlap interference. However, its robustness in high-noise environments remains limited. Pruthi et al. (2020) employed a firefly optimisation algorithm to enhance noise handling and improve nonlinear fitting performance; however, the method's sensitivity to initial parameters and its environmental adaptability still require further refinement. Dong et al. (2021) introduced Ellipse R-CNN, which leverages convolutional neural networks and clustering techniques to enhance fitting accuracy. However, its heavy reliance on large amounts of labelled data poses significant challenges. Although Ou et al. (2021) optimised the model to reduce data dependency, the computational complexity remains high, limiting its efficiency in real-time applications.

To improve consistency in ellipse detection, Wang et al. (2024) proposed the Anisotropic Scale-Invariant method, which normalises ellipses to a unit circle in the ellipse normalisation (EN) space to handle ellipses of varying sizes and shapes. However, this approach's reliance on EN space transformation increases computational overhead, and its performance with extremely elliptical shapes remains unverified. Wang et al.'s (2022) EIDet incorporates edge fusion and customised loss functions, significantly enhancing detection accuracy, yet its dependency on edge information and complex module design limits its applicability in resource-constrained environments. Long et al.'s (2023) three-stage robust ellipse fitting algorithm reduces manual intervention through adaptive outlier removal and polar coordinate detection, but it faces challenges due to its complexity and sensitivity to parameter selection. Jia et al.'s (2024) EDNet improves detection accuracy through optimised loss functions and edge detection modules, but its intricate network structure and reliance on edge information still require further refinement.

Duan et al. (2020) introduced a biomimetic visual control system that simulates natural visual mechanisms to enhance adaptability to complex celestial trajectories, while Toso et al. (2019) presented a QR updating factorisation method that supports real-time fitting through fast computation. However, its generalisability across broader application scenarios remains to be validated. Overall, current ellipse

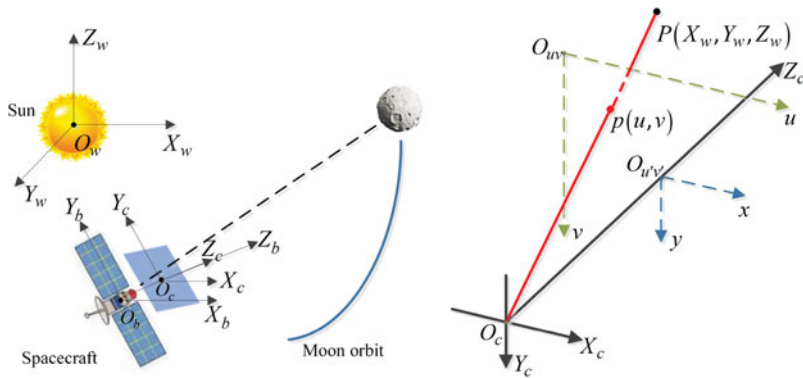


Figure 1. Relationship between the five coordinate systems.

fitting methods face challenges in balancing the complexities of handling overlaps, noise interference, and computational efficiency.

1.2. Proposed approach

To overcome the limitations of existing methods, this paper introduces an ellipse fitting technique based on a hybrid genetic algorithm for the OpNav system. By combining the global search capabilities of genetic algorithms with local optimisation strategies, this method effectively addresses challenges posed by outliers and noise, while ensuring rapid convergence to optimal solutions. The key innovations of this approach include: (1) a fast method for identifying valuable celestial contours based on edge gradients, (2) outlier elimination during the rough estimation phase using the RANSAC algorithm, and (3) improved accuracy and efficiency in celestial model computation during the refined estimation phase with the hybrid genetic algorithm.

2. Fundamentals of OpNav

2.1. Coordinate systems and LOS pointing model

The OpNav system involves five coordinate systems: the inertial coordinate system, $O_w - X_w Y_w Z_w$, the body coordinate system, $O_b - X_b Y_b Z_b$, the camera coordinate system, $O_c - X_c Y_c Z_c$, the image coordinate system, $O_{u'v'} - xy$, and the pixel coordinate system, $O_{uv} - uv$. As shown in Figure 1, the $O_w - X_w Y_w Z_w$ is used to describe the spatial position and attitude of both the celestial body and the spacecraft. The conversion relationship between the $O_b - X_b Y_b Z_b$ and the $O_c - X_c Y_c Z_c$ is determined by the camera’s mounting position. The $O_{u'v'} - xy$ and the $O_{uv} - uv$ are in the same image plane.

Based on the monocular camera, the OpNav system extracts the LOS vector from the camera to the planetary centroid. To simplify the calculation, the $O_{u'v'} - xy$ is introduced into the model. The $O_{u'v'} - xy$ and the $O_{uv} - uv$ lie in the same plane, but their origins and coordinate units differ. The point $p(x, y)$ in the $O_{u'v'} - xy$ can be expressed in pixel coordinates as

$$\begin{cases} x = (u - u')/dx \\ y = (v - v')/dy \end{cases} \tag{1}$$

where (u, v) are the pixel coordinates of the navigation object, (u', v') are the coordinates of the image plane centre, and dx and dy denote the number of pixels per unit of physical size along the respective coordinate axes. Based on the geometric relationship of the small-aperture imaging model, the relationship between the point $P(X_i, Y_i, Z_i)$ in the $O_c - X_c Y_c Z_c$ and the point $p(x_i, y_i)$ in the

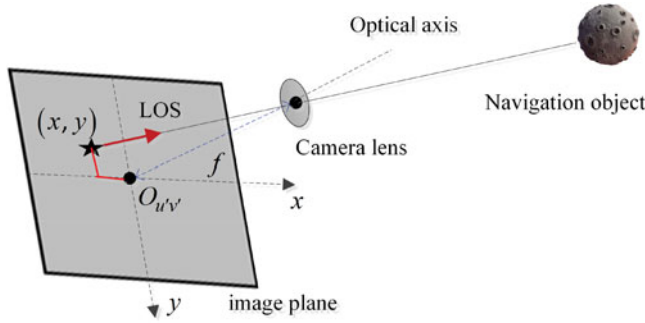


Figure 2. Imaging process and LOS direction model.

$O_{u'v'}$ – xy is given by

$$\begin{cases} x_i = f \frac{X_i}{Z_i} \\ y_i = f \frac{Y_i}{Z_i} \end{cases} \tag{2}$$

where f denotes the focal length of the camera, which is considered constant. Figure 2 illustrates the concept for estimating the optical observation LOS using image coordinates (x, y) . If the Z_c axis of the $O_c - X_c Y_c Z_c$ is assumed to coincide with the navigation camera’s optical axis, the relationship between the focal length, a measured point on the image plane, and the LOS vector to the image source is given by (Christian, 2010) the following:

$$e_i^C = \frac{1}{\sqrt{x_i^2 + y_i^2 + f^2}} \begin{bmatrix} -x_i \\ -y_i \\ f \end{bmatrix} \tag{3}$$

where e_i^C is the LOS vector in the $O_c - X_c Y_c Z_c$. Further, the LOS vector in the $O_w - X_w Y_w Z_w$ can be obtained by the rotation operation:

$$e_i^I = T_B^I T_C^B e_i^C \tag{4}$$

where T_C^B is the conversion matrix from the camera frame to the body frame, and T_B^I is the conversion matrix from the body frame to the inertial frame.

2.1. Principle of OpNav

OpNav uses the camera to determine the spacecraft’s position relative to the planet. However, determining the location using image data is an abstract process. Therefore, this section discusses the projection of a triaxial ellipsoid onto the image plane.

For a two-dimensional (2D) conic curve, the implicit equation is given by

$$Ax_i^2 + Bx_i y_i + Cy_i^2 + Dx_i + Ey_i + F = 0 \tag{5}$$

where (x_i, y_i) is the planetary edge in the image plane. If $4AC > B^2$, the curve is an ellipse. Based on the relationship between a point (x_i, y_i) in the image plane and the corresponding point (X_i, Y_i, Z_i) in the camera coordinate system, as described by Equation (2), the three-dimensional form of the model is

$$A \left(f \frac{X_i}{Z_i} \right)^2 + B \left(f \frac{X_i}{Z_i} \right) \left(f \frac{Y_i}{Z_i} \right) + C \left(f \frac{Y_i}{Z_i} \right)^2 + D \left(f \frac{X_i}{Z_i} \right) + E \left(f \frac{Y_i}{Z_i} \right) + F = 0 \tag{6}$$

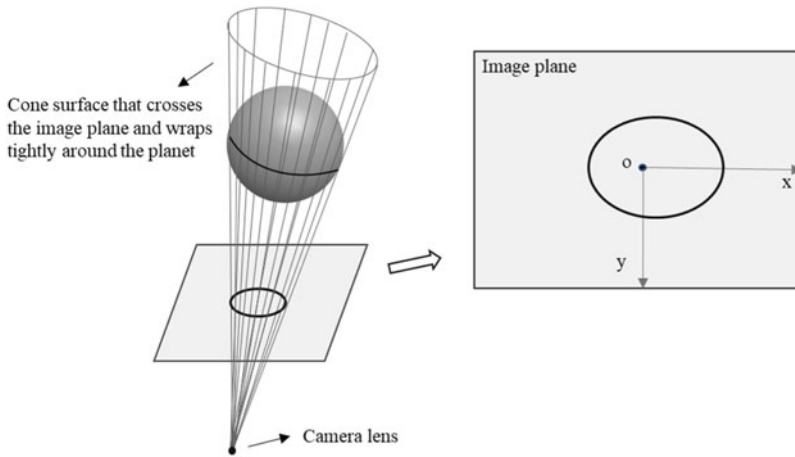


Figure 3. The process of planetary projection into the image plane.

Rewritten into matrix form as

$$[X_i \ Y_i \ Z_i] \begin{bmatrix} Af^2 & Bf^2/2 & Df/2 \\ Bf^2/2 & Cf^2 & Ef/2 \\ Df/2 & Ef/2 & F \end{bmatrix} \begin{bmatrix} X_i \\ Y_i \\ Z_i \end{bmatrix} = 0 \tag{7}$$

The P_i and K are defined as

$$P_i = [X_i \ Y_i \ Z_i]^T, \quad K = \begin{bmatrix} Af^2 & Bf^2/2 & Df/2 \\ Bf^2/2 & Cf^2 & Ef/2 \\ Df/2 & Ef/2 & F \end{bmatrix} \tag{8}$$

Then,

$$P_i^T K P_i = 0 \tag{9}$$

It can be found that Equation (9) represents a conic surface. This implies that the image plane intersects the conic surface, resulting in an ellipse, which corresponds to the planetary 2D model in the image plane (as shown in Figure 3).

After deriving the conic surface from Equation (9), the relationship with the triaxial ellipsoid representing the observed planet is established. In the planet’s inertial frame, any point P_i on its surface can be written as

$$P_i^T \begin{bmatrix} 1/a^2 & 0 & 0 \\ 0 & 1/b^2 & 0 \\ 0 & 0 & 1/c^2 \end{bmatrix} P_i = P_i^T A_P P_i = 1 \tag{10}$$

Based on the rotation matrix T_C^P from the camera to the planetary inertial frame, Equation (10) is expressed in the camera frame as

$$p_i^T T_C^P A_P (T_C^P)^T p_i = p_i^T A p_i = 1 \tag{11}$$

where p_i is the point in the camera frame corresponding to P_i . As shown in Figure 4, the vector from the origin of the camera frame to the planetary point, p_i , is given by

$$s_i = p_i - r = k e_i \tag{12}$$

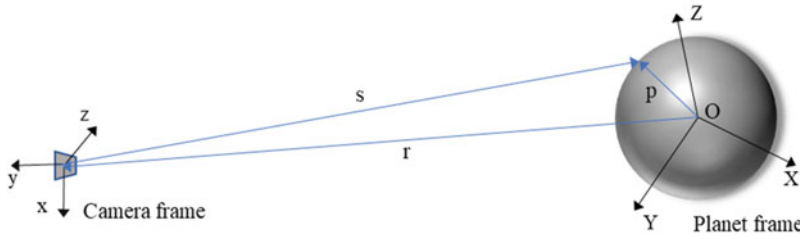


Figure 4. Geometry of the planetary surface as observed from the camera frame.

where e_i is the unit vector of s_i and k is the corresponding length. Substituting Equation (12) into Equation (11) yields

$$(e_i^T A e_i)k^2 + 2(e_i^T A r)k + (r^T A r - 1) = 0 \tag{13}$$

If k is the only real solution, it implies that the point p_i lies on the horizon. Therefore, the determining equation of Equation (13) is obtained as

$$4(e_i^T A r)^2 - 4(e_i^T A e_i)(r^T A r - 1) = 0 \tag{14}$$

Rewritten as

$$e_i^T [A r r^T A - (r^T A r - 1)A] e_i = 0 \tag{15}$$

If $M = A r r^T A - (r^T A r - 1)A$, substitute it into Equation (15) and multiply k^2 both sides of the equation by

$$s_i^T M s_i = 0 \tag{16}$$

It has been demonstrated that all possible s_i form a cone, and this conic surface is consistent with the one described by Equation (9). Therefore, if the 2D ellipse parameters are known, the position relative to the observed planet can be calculated using the projection relation. Note that A consists of the rotation matrix, which can be accurately determined using the spacecraft’s attitude and the planetary ephemeris.

3. RANSAC

To extract the centroid of an object, the celestial body is modelled as a general ellipse model:

$$F(x, y) = Ax^2 + Bxy + Cy^2 + Dx + Ey + F = 0 \tag{17}$$

where $F(x, y)$ describes an ellipse when $4AC > B^2$. It can be expressed in matrix form as

$$\begin{bmatrix} x & y & 1 \end{bmatrix} \begin{bmatrix} A & B/2 & D/2 \\ B/2 & C & E/2 \\ D/2 & E/2 & F \end{bmatrix} \begin{bmatrix} x \\ y \\ 1 \end{bmatrix} = 0 \tag{18}$$

Rewritten as

$$v^T \alpha = 0 \tag{19}$$

where $v = [x^2 \ xy \ y^2 \ x \ y \ 1]^T$ and $\alpha = [A \ B \ C \ D \ E \ F]^T$. When all points, (x_i, y_i) , lie on the ellipse, $F(x_i, y_i) = 0$. Thus, the problem is converted to

$$\min J = \sum_{i=1}^n [F(x_i, y_i)]^2 = v^T \alpha^T \alpha v \tag{20}$$

Before introducing the RANSAC method for solving J_{\min} , some essential parameters are defined. The set \mathbb{S} represents all edge points, or the sample space, while $S \in \mathbb{S}$ denotes a subset of sample points used to fit the ellipse model. The ellipse model space, represented as M , contains all model instances $M_i := M(S_i) \in M, i = 1, 2, \dots, m$. The function $d_i := \mathcal{F}(M_i, \mathbb{S})$ is defined as the distance function between a model instance, M_i , and the sample space, \mathbb{S} . Based on the distance information, the number of inliers, $N_{in}(M_i) := \sum d_i \leq \tau, i = 1, 2, \dots, m$, within the model, M_i , can be calculated, where $\tau \in R^+$ is the threshold.

The objective of RANSAC is to identify the optimal model, $M^*(S)$, which corresponds to the model $M^*(S)$ with the maximum number of inliers, $N_{in}^*(M)$. During the iterative process, each model M_i is selected with equal probability. For example, a sample S_k is chosen from the uniformly distributed sample space \mathbb{S} . The model instance, $M(S_k)$, that produces the set $N_{in}^k := N_{in}(M(S_k))$ with the highest number of inliers, that is, $N_{in}^k \geq N_{in}(M_i)$ for all i , is the desired model. It is important to note that the optimal model, $M^*(S)$, and the threshold, τ , are closely related: $M^*(S) = \tau M(S_k)$, indicating that the model is determined based on the threshold τ . The RANSAC procedure is outlined in Algorithm 1.

By minimising J , the optimal model, $M^*(S)$, is determined. As detailed in Appendix A, other essential ellipse parameters can be derived, including the centre coordinates, (x_0, y_0) , semi-major axis, a , the semi-minor axis, b , and the orientation, ϕ ,

$$\begin{cases} x_0 = \frac{2CD - BE}{B^2 - 4AC} \\ y_0 = \frac{2AE - BD}{B^2 - 4AC} \end{cases} \tag{21}$$

$$a = \sqrt{\frac{2[AE + CD - BDE + F]}{(B^2 - 4AC) \left[A + C - \sqrt{(A - C)^2 + B^2} \right]}} \tag{22}$$

$$b = \sqrt{\frac{2[AE + CD - BDE + F]}{(B^2 - 4AC) \left[A + C + \sqrt{(A - C)^2 + B^2} \right]}} \tag{23}$$

$$\phi = \frac{1}{2} \tan^{-1} \left(\frac{B}{A - C} \right) \tag{24}$$

4. Centroid extraction based on a hybrid genetic algorithm

Ellipse model fitting is a complex nonlinear problem due to the strong correlation among ellipse parameters. The RANSAC algorithm, while useful, tends to converge to local optima when addressing nonlinear problems. In such cases, the genetic algorithm has proven to be highly effective for solving ellipse models.

In OpNav tasks, various types of noise are often introduced into the original image, making it challenging for the algorithm to accurately compute the ellipse model in the presence of noise. Therefore, it is necessary to remove outliers before fitting the ellipse model. Eliminating these outliers significantly improves the performance of the method.

4.1. Outlier elimination

The process of outlier elimination involves dividing the edge points into two categories: inliers, which provide useful data for fitting the ellipse model, and outliers. Proximity information between edge points is used to capture the characteristics of the data, offering a reliable basis for outlier elimination. The Euclidean distance is employed to quantify proximity and facilitate the removal of outliers. The procedure is as follows:

Algorithm 1: The RANSAC ellipse fitting algorithm

```

1:  $N_{in}^*(M) := \{ \}$  ,  $M^*(S) := \{ \}$ 
2: for  $i := 1$  to  $I$  do
3:   Choose  $S_i^1, \dots, S_i^k \sim \mathbb{S}$ 
4:    $M_i^1, \dots, M_i^k \sim M := fitting(S_i^1, \dots, S_i^k)$ 
5:    $N_{in}(M_i^1), \dots, N_{in}(M_i^k) := computing(M_i^1, \dots, M_i^k \sim M)$ 
6:   if  $N_{in}(M_i) > N_{in}^*(M)$  then
7:      $N_{in}^*(M) := N_{in}(M_i)$ 
8:      $M^*(S) := M_i$ 
9:   end if
10: end for
11: return  $\{N_{in}^*(M), M^*(S)\}$ 

```

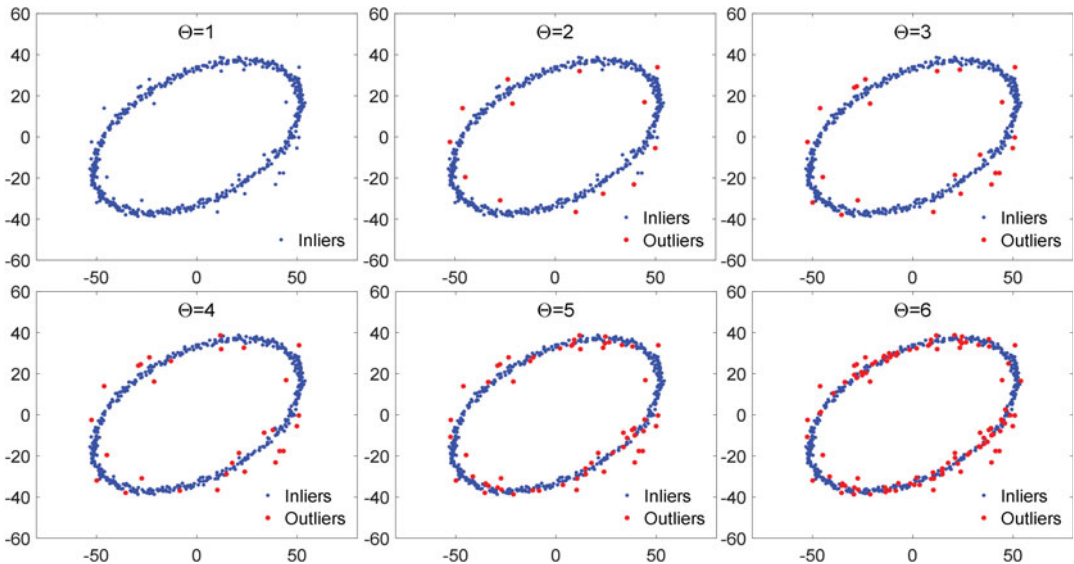


Figure 5. Results of outlier elimination trials for different thresholds Θ ($\Theta \in [1, 6]$).

- 1) Construct a proximity information space \mathbb{Z} to store the proximity data, $Z_{ij} = \|(x_i, y_i), (x_j, y_j)\|$, between point (x_i, y_i) and point (x_j, y_j) ;
- 2) Count the number, k_i , of neighbouring points around the point (x_i, y_i) based on the proximity information space, \mathbb{Z} ;
- 3) Set a threshold, Θ , to determine whether a point (x_i, y_i) is an outlier, assuming $k_i < \Theta$.

The threshold Θ significantly affects the performance of the outlier elimination process. When Θ is too small, sample points tend to form strong connections, making it difficult to detect outliers. Conversely, when Θ is too large, inliers within the sample space, \mathbb{S} , are more likely to be considered outliers. Therefore, careful selection of the threshold value is crucial. Six sets of comparative trials were conducted to determine the optimal value of Θ . In these tests, the range of integer values for Θ was $\Theta \in [1, 6]$. The results, presented in Figure 5, indicated that the best performance for outlier rejection was achieved when $\Theta = 3$. Almost all outliers were accurately detected, with no inliers excluded. Thus, the optimal threshold for the outlier elimination process was $\Theta = 3$.

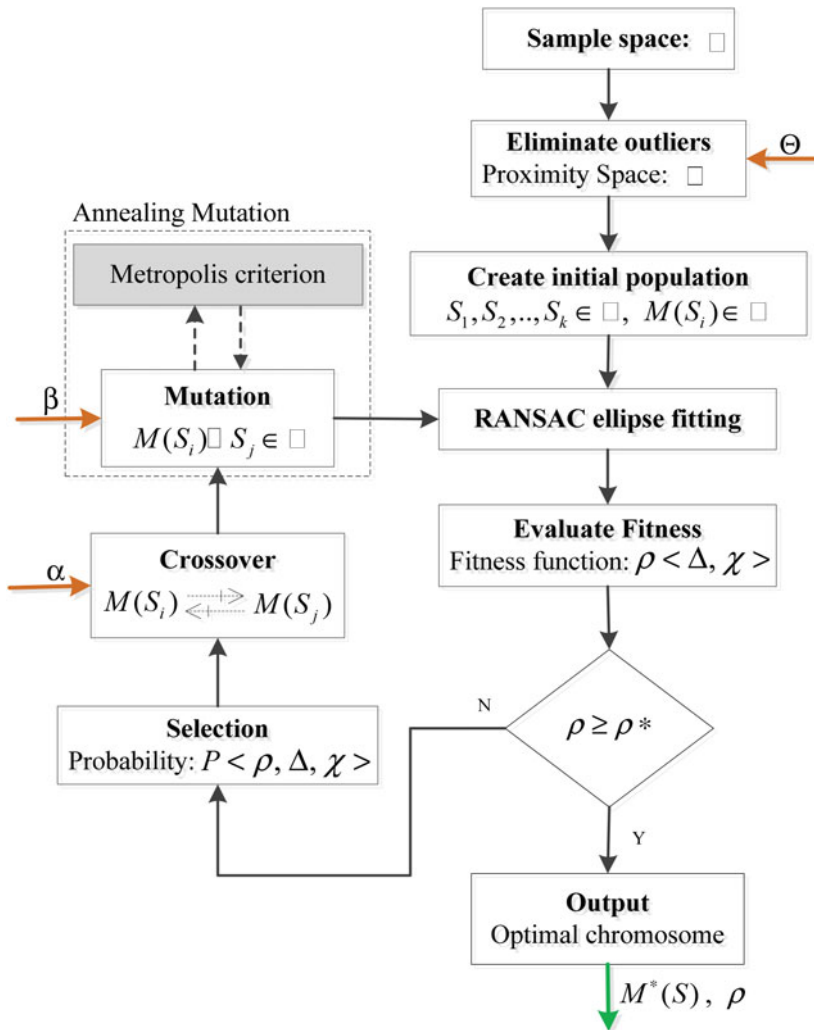


Figure 6. Overview of the method: orange arrows represent inputs, and green arrows represent outputs.

4.2. Finding the optimal model using a hybrid genetic algorithm

The genetic algorithm is a stochastic search method that simulates biological evolution. It aims to identify individuals with high fitness through selection, crossover, and mutation operations. In this problem, the chromosome in the hybrid genetic algorithm represents the ellipse model, with the points on the ellipse functioning similarly to genes in a chromosome. Given that an ellipse model can be fitted using multiple pixel points, this approach innovatively treats the pixel points as genes, facilitating the solution of the ellipse model within the hybrid genetic algorithm framework. This strategy eliminates the need for traditional gene encoding and decoding processes, significantly improving computational efficiency. The complete procedure of the hybrid genetic algorithm is illustrated in Figure 6.

In the current application, the initialisation operation randomly selects 180 points from the sample space, \mathbb{S} , to construct the model population, M . Using these edge points, 30 chromosomes (ellipse models $M_i \in M$) are generated as the initial population, with each chromosome consisting of 6 genes (edge points $(x_i, y_i) \in \mathbb{S}$). It is important to note that the outlier elimination procedure is performed before this step.

After the outlier elimination operation, it is assumed that the sample space $\mathbb{S}' \in \mathbb{S}$ consists of normal data. A model, M_i , that includes a higher number of inliers typically corresponds to a lower error. Therefore, the performance of an ellipse model M_i can be evaluated based on the number of inliers, $N_{in}(M_i)$. However, it is also important to consider the distribution of outliers around the model. The fitness evaluation function, ρ , is defined as follows:

$$\begin{aligned} \rho &= \Delta * \chi \\ &= \frac{\left| N_{in}(M_i) - \frac{1}{n} \sum_{i \leq n} S_{in}(M_i) \right|}{|\mathbb{S}|} \exp \left(-\frac{1}{2} \left[\frac{\mathcal{F}(M_i, \mathbb{S})}{\tau} \right]^2 \right) \end{aligned} \tag{25}$$

where Δ is the reward function used to evaluate the number of inliers, and χ is the distance scale function employed to assess the distribution of outliers around the model. The maximum value of the χ function is 1, indicating that the current model represents an optimal solution.

During the selection operation, the probability of selecting an individual is proportional to its fitness. This strategy has the advantage of automatically identifying better-performing individuals while ensuring that no individuals in the population are discarded. The probability, P , of selecting an individual is given by

$$P_i = \frac{|a \cdot \rho_{\Delta}^i + b \cdot \rho_{\chi}^i|}{\sum_{j=1}^n \sqrt{(a \cdot \rho_{\Delta}^j + b \cdot \rho_{\chi}^j)^2}} \tag{26}$$

where a and b denote the factors of the reward function, ρ_{Δ} , and the distance scale function, ρ_{χ} , respectively. The properties of the selection operation can be controlled by adjusting these two factors.

The crossover of two chromosomes is designed to evolve better individuals. Since edge points are treated as the genes of a chromosome, crossover is achieved by swapping points between individuals. Parental chromosomes are randomly mated to produce two offspring chromosomes. A crossover factor, α , is introduced to control the crossover point between genes, with its value set in the range of $\alpha \in (0, 1)$. In each crossover event, the parental chromosomes mate only once.

The original mutation method is a one-way, random operation, which often causes the algorithm to converge to locally optimal results. To improve the performance of the mutation operation, an annealing mutation operator is introduced, which operates in a two-way, probabilistic manner. The mutation factor, β , is used to control the mutation probability, with its value set in the range of $\beta \in (0, 1)$. Mutation results are either accepted or rejected based on the improved Metropolis criterion. If $\rho_{i+1} > \rho_i$, the probability of accepting the new variant result is 1. Otherwise, the acceptance probability is determined using the distance scale function, χ , of the outliers. The improved Metropolis criterion is defined as

$$\text{Improved Metropolis} := \begin{cases} 1, & \rho_{i+1} > \rho_i \\ \exp \left(-\frac{1}{2} \left(\frac{\rho_{i+1}}{\rho_i} \right)^2 \right), & \rho_{i+1} < \rho_i \end{cases} \tag{27}$$

5. Simulation and analysis

5.1. α, β test

Before evaluating the performance of the algorithm, it is necessary to determine the optimal crossover parameter, α , and the annealing mutation parameter, β . The crossover parameter, α , controls the mating operations between two chromosomes, enabling the population to evolve into better individuals. The annealing mutation parameter, β , is introduced to prevent the algorithm from converging to a local optimum.

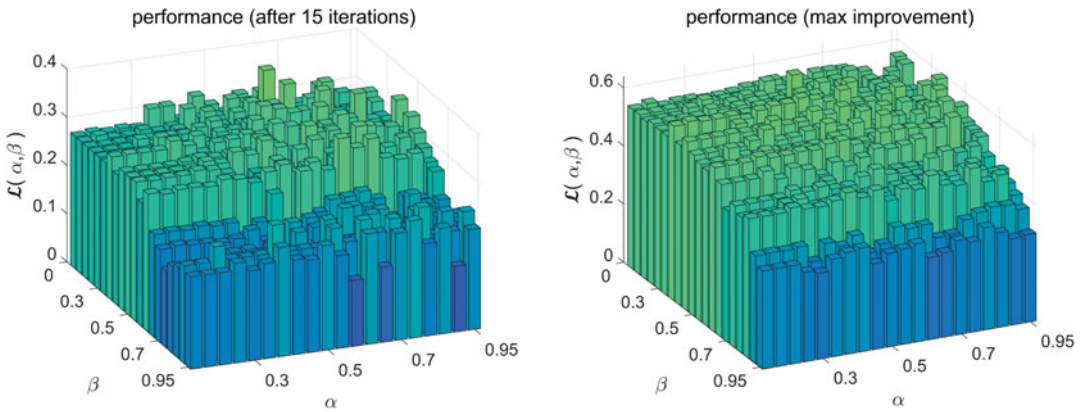


Figure 7. Relative goodness tests are performed to determine a pair of coupled parameters: the crossover parameter, α , and the annealing mutation parameter, β .

The general performance analysis of the method is based on the following terms. The inlier function, G , calculated using the parameters α, β , is denoted as

$$G_t(\alpha, \beta) := N_{in}^t(M_{\alpha, \beta}) \tag{28}$$

The average performance curve, L , is defined as

$$L_t(\alpha, \beta) := \frac{G_t(\alpha, \beta)}{m} = \frac{1}{m} \sum_{i=1}^m N_{in}^t(M_i) \tag{29}$$

$L_t(\alpha, \beta)$ represents the average number of inliers in the evolutionary process of the algorithm at time t . It reflects the average performance of the algorithm during its evolution. The parameters α and β in the algorithm exhibit a degree of coupling, and it is important to consider the impact of this pair of parameters on the algorithm’s performance. Therefore, the relative goodness curve, \mathcal{L} , is defined to represent the performance graph:

$$\mathcal{L}(\alpha, \beta) := \frac{L(\alpha, \beta) - \min_{\forall \alpha', \beta'} G(\alpha', \beta')}{\max_{\forall \alpha', \beta'} G(\alpha', \beta') - \min_{\forall \alpha', \beta'} G(\alpha', \beta')} \tag{30}$$

In the test, the parameter ranges for α and β are set as $(0, 0.95]$. The performance of \mathcal{L} (as shown in Figure 7) improves significantly after several iterations. Specifically, the maximum value of \mathcal{L} increases from 0.3824 in the fifteenth generation to a peak value of 0.6384 . As a result, the optimal values for the parameters were found to be $\alpha = 0.55$ and $\beta = 0.15$.

5.2. Ellipse fitting test

The edge points of the ellipse are used to evaluate the performance of the algorithm. To test its accuracy and robustness, various levels of Gaussian noise are introduced into the data. The standard deviations, Δ , of the Gaussian noise are set to $0.3, 1, 1.5,$ and $2,$ respectively. After the iterative process, the results are shown in Figures 8–11. The experimental results demonstrated that the proposed method achieved superior accuracy and robustness. As noted previously, RANSAC tends to converge to a local optimum as noise levels increase. In contrast, the proposed method consistently and accurately extracted the centroid of the ellipse model.

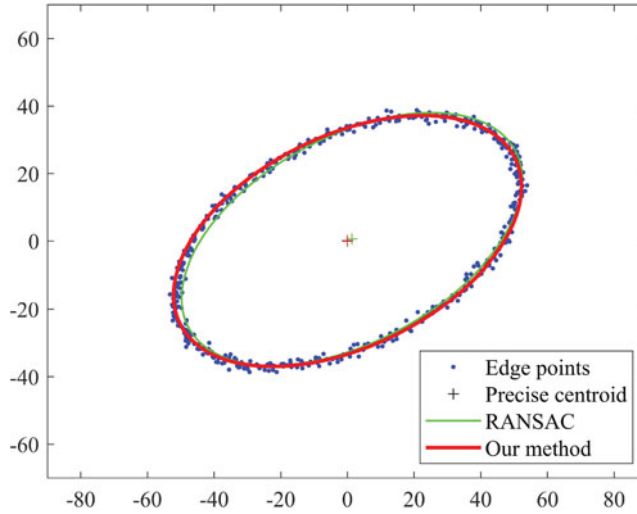


Figure 8. RANSAC and the proposed method utilise edge points to fit the ellipse model ($\Delta = 0 \cdot 3$).

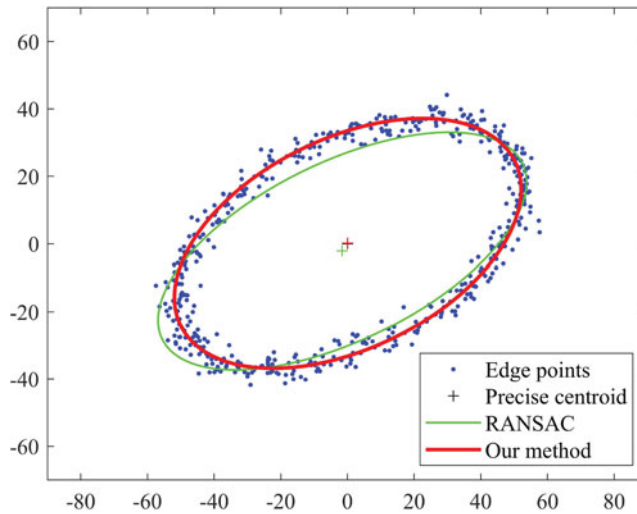


Figure 9. RANSAC and the proposed method utilise edge points to fit the ellipse model ($\Delta = 1$).

The number of inliers involved in the ellipse model is shown in Figure 12, where the total number of edge points is 506. The results indicated that the outlier elimination operation effectively mitigated the impact of noise. Furthermore, the ellipse models computed by the proposed method incorporated nearly all valuable edge points. Consequently, the precision and robustness of this approach outperformed those of RANSAC.

The statistical results of the comparison test are presented in Table 1. The minimum fitting error for RANSAC was $0 \cdot 671582$ pixels, while the maximum error reached $2 \cdot 462185$ pixels. In contrast, the maximum fitting error of the proposed method was $0 \cdot 190068$ pixels, demonstrating that the proposed approach for deep space OpNav yielded superior performance in celestial centroid extraction. However, the accuracy of centroid extraction does not directly reflect the overall performance of the OpNav system. To assess this, the LOS direction for OpNav must be computed according to Equation (3).

For this evaluation, the camera parameters are assumed to be a focal length of $f = 200$ mm, a field of view of $\vartheta = 3 \cdot 5^\circ$, and scale factors of $dx = 78 \cdot 4$ pixel/mm and $dy = 68 \cdot 7$ pixel/mm. The LOS

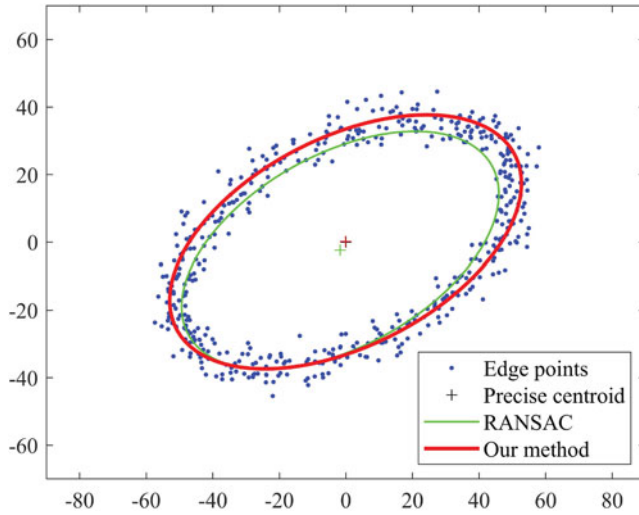


Figure 10. RANSAC and the proposed method utilise edge points to fit the ellipse model ($\Delta = 1 \cdot 5$).

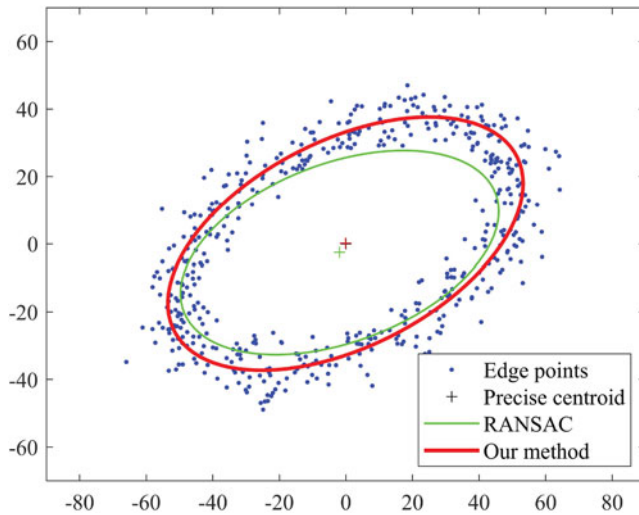


Figure 11. RANSAC and the proposed method utilise edge points to fit the ellipse model ($\Delta = 2$).

Table 1. Errors of the planetary centroid.

Comparison of two methods		Ellipse fitting errors of the planetary centroid (pixel)			
		The standard deviation of Gaussian noise:			
		$\Delta = 0 \cdot 3$	$\Delta = 1$	$\Delta = 1 \cdot 5$	$\Delta = 2$
RANSAC	x_0 coordinate error	1 · 340141	-1 · 564522	-1 · 711254	-1 · 892337
	y_0 coordinate error	0 · 671582	-2 · 123813	-2 · 352374	-2 · 462185
Our method	x_0 coordinate error	0 · 016472	0 · 096484	-0 · 110343	-0 · 141847
	y_0 coordinate error	0 · 121552	0 · 168122	0 · 172195	0 · 190068

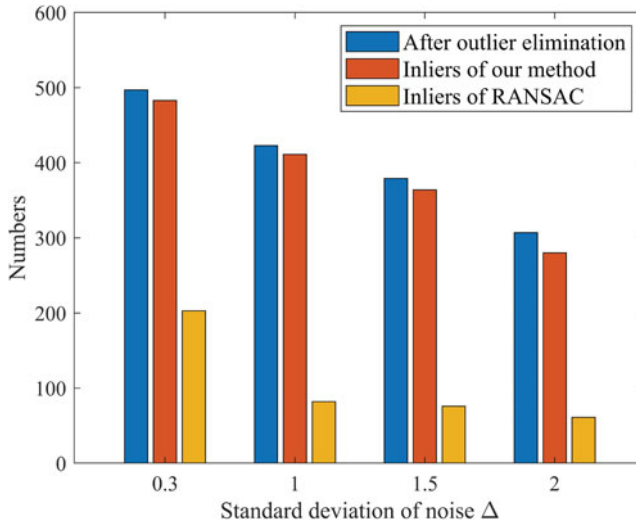


Figure 12. Comparison of the number of inliers between RANSAC and the proposed method under different levels of Gaussian noise.

Table 2. Errors of the LOS direction.

Comparison of two methods	Errors in the LOS direction from the camera to the raw image (10^{-4} rad)			
	The standard deviation of Gaussian noise:			
	$\Delta = 0.3$	$\Delta = 1$	$\Delta = 1.5$	$\Delta = 2$
RANSAC	0.987811	1.85706	2.04953	2.18025
Our method	0.0902536	0.138414	0.145183	0.166826

pointing accuracy for OpNav is shown in Table 2. The results indicated that the LOS direction errors of the proposed method were less than 0.902536×10^{-5} rad under noise $\Delta = 0.3$, and less than 1.66826×10^{-5} rad under noise $\Delta = 2$, both of which are smaller than the corresponding errors of the RANSAC method.

Next, the centroid extraction errors of the two methods were compared under varying levels of noise. Both approaches used edge points with different noise levels to fit ellipse models, and the results are presented in Figure 13. As the standard deviation, Δ , of the noise increased, the fitting errors for both methods also increased. However, it was evident that the fitting error of the proposed method gradually decreased to a small value as the number of iterations grew. Due to the diverse population in the algorithm, the proposed method consistently demonstrated smaller fitting errors compared to RANSAC. In conclusion, the proposed method not only accurately extracted the planetary centroid but also effectively mitigated the impact of noise.

To simulate realistic OpNav scenarios, celestial images were used to evaluate the performance of the two algorithms. These images were generated using Celestia, an authoritative software developed by NASA. Three images of a planet from different scenes were considered, with varying levels of Gaussian noise ($\Delta = 5, 10, 25$) were added to the images. The results of the two methods are shown in Figures 14–16. The position of the celestial centroid is located at the centre of the image, marked by the white spot. It can be observed that the proposed method accurately extracted the celestial centroid, even

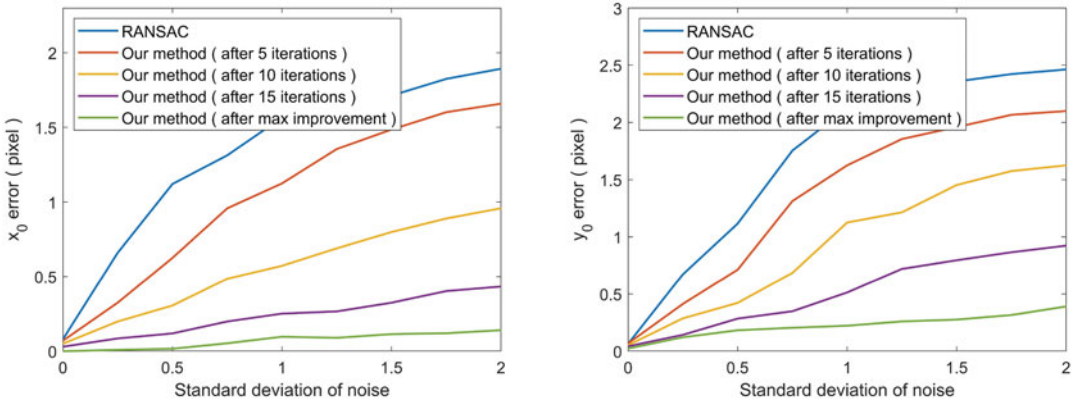


Figure 13. Errors in the x_0 and y_0 coordinates of centroid extraction under different noise levels.



Figure 14. Results of RANSAC (green) and the proposed method (red) for fitting planetary images. The white spot is the precise centroid ($\Delta = 5$).



Figure 15. Results of RANSAC (green) and the proposed method (red) for fitting planetary images. The white spot is the precise centroid ($\Delta = 10$).



Figure 16. Results of RANSAC (green) and the proposed method (red) for fitting planetary images. The white spot is the precise centroid ($\Delta = 25$).

under different noise levels. Therefore, the effectiveness of the proposed method was demonstrated, making it suitable for application in deep space OpNav.

6. Conclusions

This paper presents a robust optical observation extraction method for deep space exploration, based on a hybrid genetic algorithm. By incorporating proximity information, the method effectively reduced noise, while a fitness evaluation mechanism and an annealing mutation operator optimised model performance and prevented premature convergence. The proposed ellipse fitting technique leverages the global search capabilities of genetic algorithms combined with local optimisation to address challenges such as outliers and noise. Extensive testing under varying noise levels demonstrated the method's superior accuracy and robustness in centroid extraction, even under complex conditions. These advancements improve the reliability of OpNav systems, providing a promising solution for autonomous spacecraft navigation in deep space.

Acknowledgements. Many thanks to Baojun Lin and Yingchun Liu for their discussions and contributions to this work.

References

- A'Hearn, M. F., Belton, M. J. S., Delamere, W. A., McFadden, L. A., Meech, K. J., Melosh, H. J., Schultz, P. H., Sunshine, J. M., Thomas, P. C., Veverka, J., Yeomans, D. K., Baca, M. W., Busko, I., Crockett, C. J., Collins, S. M., Desnoyer, M., Eberhardy, C. A., Ernst, C. M., Farnham, T. L., Feaga, L., Groussin, O., Hampton, D., Ipatov, S. I., Li, J.-Y., Lindler, D., Lisse, C. M., Mastrodemos, N., Owen, Jr., W. M., Richardson, J. E., Wellnitz, D. D. and White, R. L. (2005). Deep impact: Excavating comet Tempel 1. *Science*, **310**(5746), 258–264.
- Albee, A. L., Arvidson, R. E., Palluconi, F. and Thorpe, T. (2001). Overview of the Mars global surveyor mission. *Journal of Geophysical Research: Planets*, **106**(E10), 23291–23316.
- Bhaskaran, S., Riedel, J., Synnott, S. and Wang, T. (2000). The Deep Space 1 Autonomous Navigation System-A Post-Flight Analysis. *Astrodynamics Specialist Conference*. p. 3935.
- Borisov, S. and Mortari, D. (2014). Optimal single-point and filtered pose estimation for lunar orbiters using visible camera.
- Cheng, Y., Johnson, A. E., Matthies, L. H. and Olson, C. F. (2003). Optical Landmark Detection for Spacecraft Navigation. *13th AAS/AIAA Space Flight Mechanics Meeting*, 224.
- Christian, J. A. (2010). Optical navigation for a spacecraft in a planetary system.
- Christian, J. A. and Lightsey, E. G. (2012). Onboard image-processing algorithm for a spacecraft optical navigation sensor system. *Journal of Spacecraft and Rockets*, **49**, 337–352.
- Dong, W., Roy, P., Peng, C. and Isler, V. (2021). Ellipse R-CNN: Learning to infer elliptical object from clustering and occlusion. *IEEE Transactions on Image Processing*, **30**, 2193–2206.
- Duan, H., Sun, Y. and Shi, Y. (2020). Bionic visual control for probe-and-drogue autonomous aerial refueling. *IEEE Transactions on Aerospace and Electronic Systems*, **57**(2), 848–865.
- Gaskell, R. W. (2011). Optical navigation near small bodies. *Advances in the Astronautical Sciences*, **140**, 1705–1717.
- Hanak, F. C. (2009). Lost in low lunar orbit crater pattern detection and identification.
- Hess, S. L., Henry, R. M., Leovy, C. B., Ryan, J. A. and Tillman, J. E. (1977). Meteorological results from the surface of Mars: Viking 1 and 2. *Journal of Geophysical Research*, **82**(28), 4559–4574.
- Jia, Q., Liu, Z., Liu, Y., Wang, Y., Xue, X. and Wang, W. (2024). Shape-Aware ellipse detection via parametric correlation learning. Available at SSRN 4861105.
- Liu, Z., Liu, X., Duan, G. and Tan, J. (2020). A real-time and precise ellipse detector via edge screening and aggregation. *Machine Vision and Applications*, **31**, 1–23.
- Long, C., Hu, Q., Zhao, M., Li, D., Ouyang, Z. and Yan, D. M. (2023). A triple-stage robust ellipse fitting algorithm based on outlier removal. *IEEE Transactions on Instrumentation and Measurement*, **72**, 1–14.
- Masursky, H. (1973). An overview of geological results from Mariner 9. *Journal of Geophysical Research*, **78**(20), 4009–4030.
- Mortari, D., D'Souza, C. N. and Zanetti, R. (2013). Image processing of illuminated ellipsoid. *Journal of Spacecraft & Rockets*, **53**(3), 1–9.
- Ou, W. L., Kuo, T. L., Chang, C. C. and Fan, C. P. (2021). Deep-learning-based pupil center detection and tracking technology for visible-light wearable gaze tracking devices. *Applied Sciences*, **11**(2), 851.
- Owen Jr, W. M. (2011). *Methods of Optical Navigation* (No. AAS 11-215).
- Panagiotakis, C. and Argyros, A. (2020). Region-based fitting of overlapping ellipses and its application to cells segmentation. *Image and Vision Computing*, **93**, 103810.
- Pruthi, J., Khanna, K. and Arora, S. (2020). Optic Cup segmentation from retinal fundus images using glowworm swarm optimization for glaucoma detection. *Biomedical Signal Processing and Control*, **60**, 102004.

Psiaki, M. and Hinks, J. (2007). Autonomous lunar orbit determination using star occultation measurements. *AIAA Guidance, Navigation and Control Conference and Exhibit* (p. 6657).

Rohrschneider, R. (2011) Terrain Relative Navigation Using Crater Identification in Surface Topography Data. *Aiaa Guidance, Navigation, & Control Conference*.

Synnott, S. P., Donegan, A. J., Riedel, J. E., et al. (1986). Interplanetary Optical Navigation - Voyager Uranus Encounter. In *Astrodynamic* 1985,.

Toso, F., Berto, M., Alberti, L., et al. (2019). Efficient QR updating factorization for sensorless synchronous motor drive based on high frequency voltage injection. *IEEE Transactions on Industrial Electronics*, **67**(12), 10213–10222.

Wang, Z., Zhong, B. and Ma, K. K. (2024). Anisotropic scale-invariant ellipse detection. *IEEE Transactions on Image Processing*, **33**, 3161–3173.

Wang, T., Lu, C., Shao, M., et al. (2022). Eldet: An Anchor-Free General Ellipse Object Detector. *Proceedings of the Asian Conference on Computer Vision*, p. 2580–2595.

A. Appendix A

Consider the general equation of a conic section:

$$Ax^2 + Bxy + Cy^2 + Dx + Ey + F = 0 \tag{A1}$$

where A, B, C, D, E, F are constants. The objective is to transform this equation into the standard form of an ellipse through coordinate transformations, including translation and rotation, and to derive the lengths of the semi-major and semi-minor axes.

A.1. Coordinate translation to eliminate linear terms

To eliminate the linear terms Dx and Ey , a coordinate translation is performed, establishing a new centre at (x_0, y_0) :

$$x = x' + x_0, y = y' + y_0 \tag{A2}$$

Substituting these into the original equation yields

$$A(x' + x_0)^2 + B(x' + x_0)(y' + y_0) + C(y' + y_0)^2 + D(x' + x_0) + E(y' + y_0) + F = 0 \tag{A3}$$

Upon expansion and simplification, the linear terms involving x' and y' appear as

$$(2Ax_0 + By_0 + D)x' + (2Cy_0 + Bx_0 + E)y' \tag{A4}$$

To eliminate these linear terms, the following conditions must be satisfied:

$$\begin{aligned} 2Ax_0 + By_0 + D &= 0(\text{for } x_0) \\ 2Cy_0 + Bx_0 + E &= 0(\text{for } y_0) \end{aligned} \tag{A5}$$

Solving this system yields the coordinates of the ellipse centre:

$$\begin{cases} x_0 = \frac{2CD - BE}{B^2 - 4AC} \\ y_0 = \frac{2AE - BD}{B^2 - 4AC} \end{cases} \tag{A6}$$

After eliminating the linear terms, the equation simplifies to

$$Ax'^2 + Bx'y' + Cy'^2 + F' = 0 \tag{A7}$$

where F' is expressed as a combination of the squares of x_0 and y_0 along with the original constant F :

$$F' = Ax_0^2 + Bx_0y_0 + Cy_0^2 + Dx_0 + Ey_0 + F \tag{A8}$$

A.2. Elimination of cross terms through coordinate rotation

To eliminate the cross term $Bx'y'$, a rotation of coordinates is performed, defined by an angle θ . The relationship between the new coordinates (x'', y'') and the old coordinates (x', y') is given by

$$x' = x'' \cos \theta - y'' \sin \theta, y' = x'' \sin \theta + y'' \cos \theta \tag{A9}$$

Substituting these into $Ax'^2 + Bx'y' + Cy'^2$ and expanding leads to the condition for eliminating the cross term $x''y''$:

$$(A - C) \sin(2\theta) + B \cos(2\theta) = 0 \tag{A10}$$

Solving for θ yields

$$\theta = \frac{1}{2} \tan^{-1} \left(\frac{B}{A - C} \right) \tag{A11}$$

A.3. Transformation to standard form

After rotation, the equation simplifies to a form without cross terms:

$$\lambda_1 x''^2 + \lambda_2 y''^2 + F' = 0 \tag{A12}$$

where λ_1 and λ_2 are defined as

$$\lambda_1 = \frac{A + C}{2} + \frac{\sqrt{(A - C)^2 + B^2}}{2}, \lambda_2 = \frac{A + C}{2} - \frac{\sqrt{(A - C)^2 + B^2}}{2} \tag{A13}$$

To achieve the standard form, the equation is divided by $-F'$:

$$\frac{x''^2}{a^2} + \frac{y''^2}{b^2} = 1 \tag{A14}$$

where the semi-major axis a and semi-minor axis b are given by

$$a = \sqrt{\frac{-F'}{\lambda_1}}, b = \sqrt{\frac{-F'}{\lambda_2}} \tag{A15}$$

A.4. Calculation of the constant term F'

The expression for F' is shown in Equation (1). Substituting x_0 and y_0 into Equation (1):

$$F' = F + \frac{(2CE - BD)^2 A + 2(2CE - BD)(2AD - BE)B + (2AD - BE)^2 C}{(B^2 - 4AC)^2} \tag{A16}$$

Ultimately, the semi-major axis a and semi-minor axis b are

$$\begin{aligned}
 a &= \sqrt{\frac{2[AE + CD - BDE + F]}{(B^2 - 4AC) \left[A + C - \sqrt{(A - C)^2 + B^2} \right]}} \\
 b &= \sqrt{\frac{2[AE + CD - BDE + F]}{(B^2 - 4AC) \left[A + C + \sqrt{(A - C)^2 + B^2} \right]}}
 \end{aligned}
 \tag{A17}$$